JGR Space Physics

RESEARCH ARTICLE
10.1029/2019JA027380

Combined Whistler Heat Flux and Anisotropy Instabilities in Solar Wind

M. Sarfraz[1] and P. H. Yoon[2,3]

[1]Department of Physics, GC University Lahore, Lahore, Pakistan, [2]Institute for Physical Science and Technology, University of Maryland, College Park, MD, USA, [3]Korea Astronomy and Space Science Institute, Daejeon, Korea

Key Points:
- Whistler heat flux and temperature anisotropy instabilities are investigated
- Interplay of forward and backward modes are studied by quasi-linear theory
- Linear theory cannot predict the dominance of forward versus backward modes

Correspondence to:
M. Sarfraz,
sarfraz_gcu@yahoo.com

Citation:
Sarfraz, M., & Yoon, P. H. (2020). Combined whistler heat flux and anisotropy instabilities in solar wind. *Journal of Geophysical Research: Space Physics*, *125*, e2019JA027380. https://doi.org/10.1029/2019JA027380

Received 6 SEP 2019
Accepted 20 NOV 2019
Accepted article online 15 DEC 2019

Abstract Whistler heat flux and electron temperature anisotropy instabilities are spontaneously generated in the expanding solar wind. The present study investigates the interplay between the two unstable modes and how each contributes to the dynamical evolution of macroscopic quantities. Whistler heat flux instability is excited in the forward direction along the heat flow, whereas anisotropy instability propagates in both backward and forward directions. Velocity moment-based quasi-linear theory is employed in order to investigate the saturation behavior of these instabilities, and it is shown that under certain conditions, the forward propagating whistler heat flux instability dominates, while for other conditions, especially when the temperature anisotropies are sufficiently high, it is shown that the backward mode may also contribute to the dynamical process, and even dominate. These saturation behaviors cannot be predicted by linear growth rate alone and that they imply that in the global-kinetic models of the solar wind, bidirectional nature of these instabilities must be carefully taken into account.

1. Introduction

In situ measurements show that solar wind electrons can be modeled with several distinct components (Maksimovic et al., 2005; Štverák et al., 2008), the dominant component being the relatively cooler core electrons. The so-called halo electrons are less dense in comparison with the core electrons, but are hot, that is, $T_h > T_c$, where T_h and T_c denote halo and core electron temperatures, respectively. The solar wind electrons can also contain highly field-aligned *strahl* component, especially for fast winds, but in the present paper we consider the strahl as part of the halo, which is a reasonable approximation for slow winds in particular. Observations also reveal the presence of relative drift between the core and halo electrons, which is particularly true if we treat the strahl as part of the halo. The relative streaming motion of the core and halo electrons (in the proton rest frame) implies that the solar wind electrons carry a net heat flux (Tong et al., 2019). The instability associated with the drift motion regulate the heat flux (Gary, 1985), which is important for the solar wind (Parker, 1964; Pontieu et al., 2011) and for astrophysical situations (Cowie & McKee, 1977).

Observations indicate that physical conditions that constrain the upper limit of total heat flux depend mainly on local parameters, which provide the motivation to explore the effects of local relaxation processes as a function of heliocentric distances—see the discussions by Gary et al. (1999), Gary and Li (2000), Tong et al. (2018), and Tong et al. (2019). The heat flux carried by the energetic electrons resides mostly along the magnetic field. A series of studies, which includes linear analysis by Gary et al. (1975), Gary et al. (1994), and Gary and Li (2000), and quasi-linear stability analysis by Gary and Feldman (1977) and Pistinner and Eichler (1998), along with numerical simulations (Komarov et al., 2018) suggest the inhibition of heat flux by pitch angle scattering of halo electrons as a result of whistler wave instability excitation.

Relative drifts higher than threshold values can excite whistler heat flux (WHF) and beaming fire hose heat flux electromagnetic instabilities for right-hand and left-hand circular polarizations, respectively. In the case of parallel propagation ($\mathbf{k} \times \mathbf{B}_0 = 0$, $\mathbf{k}$ being the wave vector and $\mathbf{B}_0$ denoting the ambient magnetic field vector) and single electron plasmas, Gary (1985) carried out a detailed dispersion analysis of WHF instability and electron beam fire hose heat flux instability generated by a relatively hot and isotropic beam in its own frame. Later, Gary et al. (1994) studied the heat flux (HF) instability for isotropic core-halo electron components and deduced the threshold conditions of this unstable mode for local and global models as well. A series of recent observations of the temperature distribution of a hot gas in galaxy clusters (Bertschinger & Meiksin, 1986; Fabian, 1994; Fang et al., 2018; Wagh et al., 2014; Zakamska & Narayan, 2003) highlighted the

contribution of these instabilities in the heat flux suppression below the collisional value. Further, assuming the isotropic core/halo electron components model, Gary and Li (2000) investigated the solar wind and other astrophysical environments that are characterized by high plasma beta, $\beta_{\|a} = 8\pi n_a T_{\|a}/B_0^2$. Here, $T_{\|a}$ is the temperature of species along the external magnetic field, and n_a is the total number density of the species labeled a.

Saeed et al. (2017) clarified the matter associated with polarization of HF instability and reported the contributions of thermal effects to stabilize the secondary and tertiary instabilities. In the companion paper, Saeed et al. (2017) highlighted a comparison between the characteristics of HF instability and electromagnetic electron cyclotron (EMEC) instability generated by different mechanisms. Recently, Shaaban et al. (2018) studied the role of interplay between initial temperature anisotropies and relative streaming among core and beaming components to excite the beaming (or heat flux) instabilities. The interplay between the two energy sources in the forms of thermal anisotropies and relative drifts of core/halo electrons has shown to have a significant influence on the dispersion characteristics of the unstable modes (Shaaban, Lazar, & Poedts, 2018; Tong et al., 2019; Vasko et al., 2019). Further, Shaaban, Lazar, Yoon, et al. (2018) refined the analysis with the inclusion of nonthermal particles which are ubiquitous in space and or in solar wind.

In the present study, we revisit the problem of combined effects of heat flux-induced and anisotropy-driven whistler instability, with the aim of highlighting the role of asymmetric or bidirectional whistler wave excitation. In the absence of temperature anisotropy, only forward propagating whistler waves are excited by the heat flux-carrying electrons. On the other hand, in the absence of the relative drift but with only temperature anisotropy, whistler wave excitation is symmetric in both forward and backward directions. When both free energy sources are available, however, the whistler wave excitation can be asymmetric such that the final state of instability development may not be so easily predicted solely within the context of linear theory alone. It turns out that high growth rate associated with either forward or backward mode does not necessarily translate into similarly high saturation amplitude, as we will see. In the present study we thus implement the quasi-linear kinetic theory under the assumption of drifting bi-Maxwellian models for the electron (and proton) velocity distribution functions and taking the velocity moments of the governing kinetic equations so as to investigate the dynamical progression of the moments, that is, average field-aligned drift speeds and temperatures, as well as the wave energy densities for the forward and backward propagating whistler waves.

We consider physical parameters guided by observation for slow solar wind conditions. The velocity moment-based quasi-linear technique was recently employed by Shaaban et al. (2019a) and Shaaban et al. (2019b) in the context of the whistler heat flux instability, but in their analyses, asymmetric or bidirectional excitation of whistler waves is not considered. Instead, they only considered the forward propagating waves. As we will see, for weak anisotropies, their approximation can be justified. However, for sufficiently high-temperature anisotropy combined with the finite heat flux, sometimes the backward whistler waves cannot be ignored. In this regard, the present analysis provides a more rigorous and comprehensive analysis. The present study constitutes a further contribution along the line of linear (Michno et al., 2014), (Maneva et al., 2016), (Shaaban et al., 2017) and quasi-linear (Sarfraz et al., 2016), (Sarfraz, 2018), (Sarfraz & Yoon, 2019), (Shaaban et al., 2019a), (Shaaban et al., 2019b) kinetic models of the solar wind, and thus the findings from the present study may be useful for comprehensive analysis of solar wind evolution.

The present paper is organized as follows: In section 2, we briefly discuss the linear and quasi-linear theory of whistler heat flux instability. Numerical solutions are presented in section 3. In section 4, we summarize the findings of the present paper.

2. Macroscopic Kinetic Model of the Solar Wind Bulk Parameters

We start our mathematical model by taking the proton velocity distribution function to be given by a bi-Maxwellian form, $f_p(v_\|, v_\perp, t) = \left[\pi^{3/2}\alpha_{\perp p}^2(t)\alpha_{\|p}(t)\right]^{-1} \exp\left[-v_\perp^2/\alpha_{\perp p}^2(t) - v_\|^2/\alpha_{\|p}^2(t)\right]$. Here, perpendicular and parallel components of the velocity defined with respect to the ambient magnetic field are represented by $v_\perp$ and $v_\|$, respectively. Further, the quantities $\alpha_{\perp p}$ and $\alpha_{\|p}$ stand for perpendicular and parallel thermal speeds of protons, defined in terms of temperatures, respectively, via $T_{\perp p}(t) = m_p \int \mathrm{d}\mathbf{v}(v_\perp^2/2) f_p = m_p \alpha_{\perp p}^2(t)/2$ and $T_{\|p}(t) = m_p \int \mathrm{d}\mathbf{v} v_\|^2 f_p = m_p \alpha_{\|p}^2(t)/2$, where m_p is the proton mass. Here, the customary Boltzmann constant is omitted in the definition for temperatures, as they are defined in the unit of energy. While the proton temperatures are fully solved in the present quasi-linear calculation, their dynamical change is

quite minimal; hence, in the subsequent presentation of numerical results, we choose not to display the proton quantities.

The core and halo electron components constitute the total electron distribution function, $f_e(v_\parallel, v_\perp, t) = (n_c/n_0)\, f_c(v_\parallel, v_\perp, t) + (n_h/n_0)\, f_h(v_\parallel, v_\perp, t)$, in which core/halo electrons are modeled by drifting bi-Maxwellians forms,

$$f_a(v_\parallel, v_\perp, t) = \frac{1}{\pi^{3/2}\alpha_{\perp a}^2(t)\alpha_{\parallel a}(t)} \exp\left(-\frac{v_\perp^2}{\alpha_{\perp a}^2(t)} - \frac{[v_\parallel - U_a(t)]^2}{\alpha_{\parallel a}^2(t)}\right), \tag{1}$$

where label $a = c, h$ is for core/halo electrons, and n_a represents the fractional number density for each species, $n_0 = \sum_{a=c,h} n_a$ being the total density. Here, U_a is parallel drift speed, satisfying the current neutrality condition, $\sum_{a=c,h} n_a U_a = 0$. Perpendicular and parallel thermal speeds for the electrons are denoted by $\alpha_{\perp a}(t)$ and $\alpha_{\perp a}(t)$, respectively. Further, the temperatures for each electron species, $T_{\perp a}(t)$ and $T_{\parallel a}(t)$, are defined in a similar way as those of the protons discussed above.

Note that the bi-Maxwellian model for halo electrons is not necessarily the most accurate form. As discussed by Shaaban, Lazar, Yoon, et al. (2018), non-Maxwellian features associated with the halo electrons, typically modeled by bi-Kappa distribution, are important. Nevertheless, in the present study, we adopt the simpler bi-Maxwellian model. Bi-Kappa modeling of the halo electrons in the context of quasi-linear analysis may be considered in the future.

Model drifting bi-Maxwellian distributions are assumed to maintain their mathematical form for all time, except that their bulk parameters, $\alpha_{\perp,\parallel a}(t)$ and $U_a(t)$ evolve in time. This is obviously an approximation, as more rigorous simulations such as those by Gary et al. (1996), Matteini et al. (2006), Hellinger et al. (2014), etc., depict some deviations of the particle distributions in the nonlinear stage of instability progression. Nevertheless, we make the above-stated assumptions for the sake of simplicity. It should be noted that such an approach is proven to provide adequate if not perfect description of the various temperature anisotropy-driven instabilities. In particular, such an approach successfully predicts the instability thresholds (Seough & Yoon, 2012), (Yoon & Seough, 2012), (Seough et al., 2013), (Sarfraz et al., 2016), (Sarfraz, 2018), (Shaaban et al., 2019b). Moreover, comparative studies between the velocity moment-based quasi-linear theory and particle-in-cell (PIC) simulations demonstrated reasonable agreement between the two methods (Seough et al., 2014), (Yoon et al., 2015), (Seough et al., 2015), (Yoon et al., 2017), (Lee et al., 2019). In particular, in a recent PIC simulation study based upon the implicit numerical scheme, López et al., 2019 analyzed the dynamical evolution of the whistler heat flux instability, and they observed that the time evolution of various velocity moments and wave magnetic field energy density behaved in accordance with quasi-linear moment calculations by Shaaban et al. (2019a) and Shaaban et al. (2019b). This provides the justification for the present simplified quasi-linear method based upon the assumption of drifting bi-Maxwellian distributions for the particles.

The parallel heat flux carried by the electrons in the proton rest frame is given by,

$$q = \frac{m_e}{2} \int \mathrm{dv}\; v_\parallel v^2 f_e. \tag{2}$$

We investigate the influence of transverse modes propagating strictly parallel or antiparallel to the ambient magnetic field on the solar wind plasma dynamics. Under this assumption, the transverse modes decouple from electrostatic oscillations. The general (nonrelativistic) dispersion relation for homogeneous and dilute (noncollisional) space plasmas is given by (Gary, 1993; Schilckeiser, 2002)

$$\frac{c^2k^2}{\omega^2} = 1 + \sum_{a=p,c,h} \frac{\omega_{pa}^2}{\omega^2} \int \mathrm{dv}\; \frac{v_\perp/2}{\omega - kv_\parallel \pm \Omega_a} \left((\omega - kv_\parallel)\frac{\partial f_a}{\partial v_\perp} + kv_\perp \frac{\partial f_a}{\partial v_\parallel}\right), \tag{3}$$

where ω and k are, respectively, angular frequency and wave number of the mode; $\omega_{pa} = (4\pi n_0 e_a^2/m_a)^{1/2}$ is the plasma frequency; $\Omega_a = e_a B_0/m_a c$ represents the cyclotron frequency of species labeled a; m_a is the mass of species labeled a; $e_a = e$ for protons and $e_a = -e$ for electrons; e is the unit electric charge; c represents the

speed of light in vacuum; n_0 stands for total number density; B_0 is the intensity of ambient magnetic field; upper and lower signs denote the right-hand versus left-hand circularly polarized electromagnetic modes, respectively. Here, the sense of left- versus right-handed circularity is defined for positive ω and k. If k is negative, then the handedness of the normal mode may flip, which we will discuss later.

Making an allowance for bi-Maxwellian distribution function defined for protons, and drifting bi-Maxwellian distribution functions for core-halo electron components (1), we obtain the dispersion relation for left- or right-hand circularly polarized mode in terms of transcendental plasma dispersion function $Z(\zeta)$ (Fried & Conte, 1961)

$$\begin{aligned}\frac{c^2k^2}{\omega_p^2} =& \frac{T_{\perp p}}{T_{\parallel p}} - 1 + \left[\frac{T_{\perp p}}{T_{\parallel p}}\,\omega_{L/R} \mp \left(\frac{T_{\perp p}}{T_{\parallel p}} - 1\right)\Omega_p\right]\frac{1}{k\alpha_{\parallel p}}\,Z\left(\frac{\omega_{L/R} \mp \Omega_p}{k\alpha_{\parallel p}}\right)\\ &+ \sum_{a=c,h}\frac{n_a}{n_0}\frac{m_p}{m_e}\left\{\frac{T_{\perp a}}{T_{\parallel a}} - 1 + \left[\frac{T_{\perp a}}{T_{\parallel a}}\left(\omega_{L/R} - kU_a\right) \pm \left(\frac{T_{\perp a}}{T_{\parallel a}} - 1\right)\Omega_e\right]\right.\\ &\left.\times\,\frac{1}{k\alpha_{\parallel a}}\,Z\left(\frac{\omega_{L/R} \mp \Omega_e - kU_a}{k\alpha_{\parallel a}}\right)\right\},\end{aligned} \tag{4}$$

where, upper/lower sign corresponds to left/right-hand or L/R mode. We have ignored the displacement current in (4), as we are not interested in fast waves (that is, we assume $ck/\omega \gg 1$ here).

The total heat flux (2) under model electron core-halo distribution (1) in the proton rest frame is given by

$$q = \sum_{a=c,h}\frac{n_a}{n_0}\frac{m_e U_a}{2}\left[\left(\frac{\alpha_{\perp a}^2}{\alpha_{\parallel a}^2} + \frac{3}{2}\right)\alpha_{\parallel a}^2 + U_a^2\right]. \tag{5}$$

Quasi-linear analysis makes use of particle and wave kinetic equations to track the evolution of velocity distributions and wave spectral intensities. Specifically, for the parallel waves and instabilities, the particle kinetic equation in the diffusion approximation, taking into account the right-hand and left-hand circularly polarized modes, is given by

$$\begin{aligned}\frac{\partial f_a}{\partial t} =& \frac{ie_a^2}{4m_a^2c^2}\frac{1}{v_\perp}\sum_{+,-}\int_{-\infty}^{\infty}\frac{\mathrm{d}k}{k^2}\left(\left(\omega^* - kv_\parallel\right)\frac{\partial}{\partial v_\perp} + kv_\perp\frac{\partial}{\partial v_\parallel}\right)\\ &\times\,\frac{v_\perp B_{L/R}^2(k)}{\omega - kv_\parallel \pm \Omega_a}\left(\left(\omega - kv_\parallel\right)\frac{\partial f_a}{\partial v_\perp} + kv_\perp\frac{\partial f_a}{\partial v_\parallel}\right),\end{aligned} \tag{6}$$

where $a = p, c, h$, $\omega = \omega_k + i\gamma_k$ is the complex root of equation (4), and $B_L^2(k)$ and $B_R^2(k)$ are the spectral wave energy densities associated with the left- versus right-hand circular polarization.

In what follows, in order to reduce the theory into *macroscopic* quasi-linear approach, we take the various velocity moments of particle kinetic equation (6). Time evolution of the velocity moments of interest are defined by

$$\begin{aligned}\frac{\mathrm{d}U_a}{\mathrm{d}t} &= \frac{\partial}{\partial t}\int \mathrm{d}\mathbf{v}\; v_\parallel f_a,\\ \frac{\mathrm{d}T_{\perp a}}{\mathrm{d}t} &= \frac{\partial}{\partial t}\int \mathrm{d}\mathbf{v}\;\frac{m_a v_\perp^2}{2} f_a,\\ \frac{\mathrm{d}T_{\parallel a}}{\mathrm{d}t} &= \frac{\partial}{\partial t}\int \mathrm{d}\mathbf{v}\; m_a v_\parallel^2 f_a.\end{aligned} \tag{7}$$

These moment equations under the application of assumed distribution functions combined with the particle kinetic equation (6) lead to the governing equations of the form

$$
\begin{aligned}
\frac{\mathrm{d}U_a}{\mathrm{d}t} &= -\frac{e^2}{2m_e^2c^2\alpha_{\|a}}\sum_{L,R}\int_0^\infty \frac{\mathrm{d}k}{k^2}\, B^2_{L/R}(k)\ \mathrm{Im}\left[P_+^{L/R} + \left(P_-^{L/R}\right)^*\right],\\
\frac{\mathrm{d}T_{\perp a}}{\mathrm{d}t} &= -\frac{e^2}{m_ec^2}\sum_{L,R}\int_0^\infty \frac{\mathrm{d}k}{k^2}\, B^2_{L/R}(k)\left[\left(\frac{2T_{\perp a}}{T_{\|a}}-1\right)\gamma_k^{L/R} + \mathrm{Im}\,\frac{2i\gamma_k^{L/R}+\Omega_e}{k\alpha_{\|a}}\, G_a^{L/R}\right],\\
\frac{\mathrm{d}T_{\|a}}{\mathrm{d}t} &= \frac{2e^2}{m_ec^2}\sum_{L,R}\int_0^\infty \frac{\mathrm{d}k}{k^2}\, B^2_{L/R}(k)\left[\frac{T_{\perp a}}{T_{\|a}}\,\gamma_k^{L/R} + \mathrm{Im}\,\frac{\omega_{L/R}+\Omega_e+kU_a}{k\alpha_{\|a}}\, G_a^{L/R}\right],\\
\frac{\mathrm{d}T_{\perp p}}{\mathrm{d}t} &= -\frac{e^2}{m_pc^2}\sum_{L,R}\int_0^\infty \frac{\mathrm{d}k}{k^2}\, B^2_{L/R}(k)\left[\left(\frac{2T_{\perp p}}{T_{\|p}}-1\right)\gamma_k^{L/R} + \mathrm{Im}\,\frac{2i\gamma_k^{L/R}-\Omega_p}{k\alpha_{\|p}}\, H_p^{L/R}\right],\\
\frac{\mathrm{d}T_{\|p}}{\mathrm{d}t} &= \frac{2e^2}{m_pc^2}\sum_{L,R}\int_0^\infty \frac{\mathrm{d}k}{k^2}\, B^2_{L/R}(k)\left[\frac{T_{\perp p}}{T_{\|p}}\,\gamma_k^{L/R} + \mathrm{Im}\,\frac{\omega_{L/R}-\Omega_p}{k\alpha_{\|p}}\, H_p^{L/R}\right],
\end{aligned}
\tag{8}
$$

with $a = c, h$ for core/halo electrons and other functions are defined by

$$
\begin{aligned}
P_+^{L/R} &= \left[\frac{T_{\perp a}}{T_{\|a}}\left(\omega_{L/R}-kU_a\right) \pm \left(\frac{T_{\perp a}}{T_{\|a}}-1\right)\Omega_e\right] Z\left(\frac{\omega_{L/R}\pm\Omega_e - kU_a}{k\alpha_{\|a}}\right),\\
\left(P_-^{L/R}\right)^* &= \left[\frac{T_{\perp a}}{T_{\|a}}\left(\omega_{L/R}+kU_a\right) + \left(\frac{T_{\perp a}}{T_{\|a}}-1\right)\Omega_e\right]^* \left[Z\left(\frac{\omega_{L/R}\pm\Omega_e + kU_a}{k\alpha_{\|a}}\right)\right]^*,\\
G_a^{L/R} &= \left[\frac{T_{\perp a}}{T_{\|a}}\left(\omega_{L/R}+kU_a\right) \pm \left(\frac{T_{\perp a}}{T_{\|a}}-1\right)\Omega_e\right] Z\left(\frac{\omega_{L/R}\pm\Omega_e + kU_a}{k\alpha_{\|a}}\right),\\
H_p^{L/R} &= \left[\frac{T_{\perp p}}{T_{\|p}}\,\omega_{L/R} \mp \left(\frac{T_{\perp p}}{T_{\|p}}-1\right)\Omega_p\right] Z\left(\frac{\omega_{L/R}\mp\Omega_p}{k\alpha_{\|p}}\right).
\end{aligned}
\tag{9}
$$

The wave-energy density equation associated with growth rate is given by

$$
\frac{\partial B^2_{L/R}(k)}{\partial t} = 2\gamma_k^{L/R} B^2_{L/R}(k). \tag{10}
$$

We choose to work in positive k space, so we need to rewrite the k integral over half space, $0 < k < \infty$. In doing so, we invoke the symmetry properties,

$$
\begin{aligned}
&\omega_L(-k) = \omega_{-k}^L + i\gamma_{-k}^L = -\omega_k^R + i\gamma_k^R = -\omega_R^*(k),\\
&\omega_R(-k) = \omega_{-k}^R + i\gamma_{-k}^R = -\omega_k^L + i\gamma_k^L = -\omega_L^*(k),\\
&B_L^2(-k) = B_R^2(k), \qquad B_R^2(-k) = B_L^2(k),\\
&Z(\zeta^*) = -[Z(-\zeta)]^*.
\end{aligned}
\tag{11}
$$

Under this treatise, R mode with positive real frequency defined over positive k space corresponds to the forward propagating whistler wave, while L mode with negative real frequency defined over positive k space corresponds to the backward propagating whistler wave. This is because the negative frequency L mode (with positive k), after implementing the symmetry relationship, becomes the positive-frequency R mode with negative k space, thus, having negative group and phase speeds. In short, the major contribution from the present study is to solve for both positive and negative real frequency solutions and adding both contributions to the evolution equations for bulk plasma parameters. Here we should note that if parallel pressure is sufficiently high, then the electron fire hose instability may be excited, which is a left-hand mode for positive k. We are not interested in the parameter regime where L mode in the positive k regime such as the electron fire hose instability is excited. As a consequence, we omit L mode for $k > 0$ at the outset.

3. Numerical Analysis

For numerical analysis we adopt the following dimensionless (normalized) variables and quantities:

$$
\begin{aligned}
&\tau = \Omega_p t, \quad z = \frac{\omega}{\Omega_p}, \quad q = \frac{ck}{\omega_{pp}}, \quad M = \frac{m_p}{m_e}, \quad \delta = \frac{n_h}{n_0}, \quad \frac{n_c}{n_0} = 1-\delta,\\
&u_h = \frac{1}{M^{1/2}}\frac{U_h}{v_A}, \quad u_c = \frac{\delta u_h}{1-\delta}, \quad \beta_{\perp p} = \frac{8\pi n_0 T_{\perp p}}{B_0^2}, \quad \beta_{\parallel p} = \frac{8\pi n_0 T_{\parallel p}}{B_0^2},\\
&\beta_{\perp c} = \frac{8\pi n_0 T_{\perp c}}{B_0^2}, \quad \beta_{\parallel c} = \frac{8\pi n_0 T_{\parallel c}}{B_0^2}, \quad \beta_{\perp h} = \frac{8\pi n_0 T_{\perp h}}{B_0^2}, \quad \beta_{\parallel h} = \frac{8\pi n_0 T_{\parallel h}}{B_0^2},\\
&A_p = \frac{T_{\perp p}}{T_{\parallel p}} - 1, \quad A_c = \frac{T_{\perp c}}{T_{\parallel c}} - 1, \quad A_h = \frac{T_{\perp h}}{T_{\parallel h}} - 1,\\
&\eta_p^{L/R} = \frac{(A_p+1)z_{L/R} \mp A_p}{q\beta_{\parallel p}^{1/2}}, \qquad \zeta_p^{L/R} = \frac{z_{L/R} \mp 1}{q\beta_{\parallel p}^{1/2}},\\
&\eta_c^{L/R} = \frac{M^{1/2}\left[(A_c+1)(z_{L/R} + M^{1/2}qu_c) \pm MA_c\right]}{q\beta_{\parallel c}^{1/2}},\\
&\zeta_c^{L/R} = \frac{z_{L/R} \pm M + M^{1/2}qu_c}{q(M\beta_{\parallel c})^{1/2}},\\
&\eta_h^{L/R} = \frac{M^{1/2}\left[(A_h+1)(z_{L/R} - M^{1/2}qu_h) \pm MA_h\right]}{q\beta_{\parallel h}^{1/2}},\\
&\zeta_h^{L/R} = \frac{z_{L/R} \pm M - M^{1/2}qu_h}{q(M\beta_{\parallel h})^{1/2}},\\
&\bar{\eta}_h^{L/R} = \frac{M^{1/2}\left[(A_h+1)(z_{L/R} + M^{1/2}qu_h) \pm MA_h\right]}{q\beta_{\parallel h}^{1/2}},\\
&\bar{\zeta}_h^{L/R} = \frac{z_{L/R} \pm M + M^{1/2}qu_h}{q(M\beta_{\parallel h})^{1/2}}, \qquad W_{L/R}(q)\,\mathrm{d}q = \frac{B_{L/R}^2(k)\,\mathrm{d}k}{B_0^2}.
\end{aligned}
\tag{12}
$$

Making use of these definitions governing equations in dimensionless form are given by

$$
\begin{aligned}
0 = {} & q^2 - A_p - (1-\delta)MA_c - \delta MA_h - \eta_p^{L/R} Z\left(\zeta_p^{L/R}\right)\\
& - (1-\delta)\eta_c^{L/R} Z\left(\zeta_c^{L/R}\right) - \delta\eta_h^{L/R} Z\left(\zeta_h^{L/R}\right),
\end{aligned}
\tag{13}
$$

which represents the instantaneous dispersion relation for L/R mode,

$$
\begin{aligned}
u_c &= \frac{\delta u_h}{1-\delta},\\
\frac{\mathrm{d}\beta_{\perp c}}{\mathrm{d}\tau} &= -\sum_{L,R}\int_0^\infty \frac{\mathrm{d}q}{q^2}\, W_{L/R}(q)\left\{2M\left(2A_c+1\right)z_i^{L/R} + 2\,\mathrm{Im}\left(2iz_i^{L/R} \pm M\right)\eta_c^{L/R} Z\left(\zeta_c^{L/R}\right)\right\},\\
\frac{\mathrm{d}\beta_{\parallel c}}{\mathrm{d}\tau} &= 2\sum_{L,R}\int_0^\infty \frac{\mathrm{d}q}{q^2}\, W_{L/R}(q)\left\{2M\left(A_c+1\right)z_i^{L/R}\right.\\
&\quad \left. +2\,\mathrm{Im}\left(z_{L/R} \pm M + M^{1/2}qu_c\right)\eta_c^{L/R} Z\left(\zeta_c^{L/R}\right)\right\},\\
\frac{\mathrm{d}u_h}{\mathrm{d}\tau} &= \frac{M^{1/2}}{2}\sum_{L,R}\int_0^\infty \frac{\mathrm{d}q}{q}\, W_{L/R}(q)\,\mathrm{Im}\left\{\eta_h^{L/R} Z\left(\zeta_h^{L/R}\right) + \left[\bar{\eta}_h^{L/R} Z\left(\bar{\zeta}_h^{L/R}\right)\right]^*\right\},\\
\frac{\mathrm{d}\beta_{\perp h}}{\mathrm{d}\tau} &= -\sum_{L,R}\int_0^\infty \frac{\mathrm{d}q}{q^2}\, W_{L/R}(q)\left\{2M\left(2A_h+1\right)z_i^{L/R} + 2\,\mathrm{Im}\left(2iz_i^{L/R} \pm M\right)\eta_h^{L/R} Z\left(\zeta_h^{L/R}\right)\right\},\\
\frac{\mathrm{d}\beta_{\parallel h}}{\mathrm{d}\tau} &= 2\sum_{L,R}\int_0^\infty \frac{\mathrm{d}q}{q^2}\, W_{L/R}(q)\left\{2M\left(A_h+1\right)z_i^{L/R}\right.\\
&\quad \left. +2\,\mathrm{Im}\left(z_{L/R} \pm M - M^{1/2}qu_h\right)\eta_h^{L/R} Z\left(\zeta_h^{L/R}\right)\right\},\\
\frac{\mathrm{d}\beta_{\perp p}}{\mathrm{d}\tau} &= -2\sum_{L,R}\int_0^\infty \frac{\mathrm{d}q}{q^2}\, W_{L/R}(q)\left\{\left(2A_p+1\right)z_i^{L/R} + \mathrm{Im}\left(2iz_i^{L/R} \mp 1\right)\eta_p^{L/R} Z\left(\zeta_p^{L/R}\right)\right\},\\
\frac{\mathrm{d}\beta_{\parallel p}}{\mathrm{d}\tau} &= 4\sum_{L,R}\int_0^\infty \frac{\mathrm{d}q}{q^2}\, W_{L/R}(q)\left\{\left(A_p+1\right)z_i^{L/R} + \mathrm{Im}\left(z_{L/R}-1\right)\eta_p^{L/R} Z\left(\zeta_p^{L/R}\right)\right\},
\end{aligned}
\tag{14}
$$

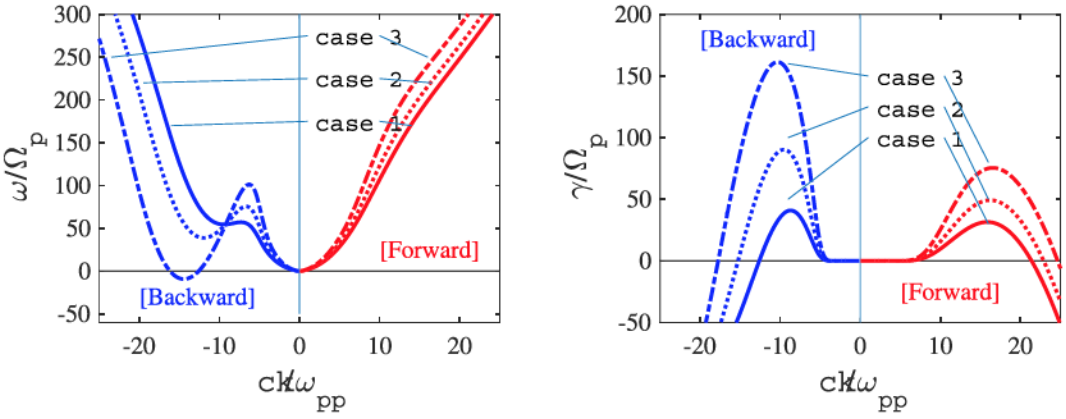

Figure 1. Initial dispersion relation. Real frequencies (left) and growth rates (right) of forward propagating whistler (red) and backward propagating whistler (blue) modes occupy positive and negative k ranges, respectively. The three cases represent different halo temperature anisotropy values.

which determine the time evolution of bulk plasma parameters, and the wave kinetic equations for L and R (or equivalently, backward and forward propagating whistler waves) are given by

$$\frac{\partial W_{L/R}(q)}{\partial \tau} = 2\gamma_i^{L/R} W_{L/R}(q). \tag{15}$$

The normalized parallel heat flux is given by

$$\begin{aligned} q_{\text{total}} &= q_c + q_h, \\ q_c &= -\frac{(1-\delta)u_c}{2}\left[\left(\frac{\beta_{\perp c}}{\beta_{\parallel c}} + \frac{3}{2}\right)\beta_{\parallel c} + u_c^2\right], \\ q_h &= \frac{\delta u_h}{2}\left[\left(\frac{\beta_{\perp h}}{\beta_{\parallel h}} + \frac{3}{2}\right)\beta_{\parallel h} + u_h^2\right]. \end{aligned} \tag{16}$$

Note that we solve for the proton betas, $\beta_{\perp p}$ and $\beta_{\parallel p}$, but as noted already, these quantities do not vary much. Consequently, in the presentation of numerical results we omit these quantities from the plot.

For illustration of the numerical analysis, let us first focus on the initial condition. In choosing the input parameters we select $\beta_{\parallel c}$, $\beta_{\parallel h}$, $\beta_{\parallel p}$, and u_h in accordance with typical values, which are frequently reported in the literature—see, for example, observational spacecraft data as reported by Pilipp et al. (1987), Maksimovic et al. (2005), Štverák et al. 2008), and Štverák et al. (2009). Figure 1 plots the numerical solution of (13) based upon the input parameters,

$$\begin{aligned} &\delta = 0.05, \quad M = 1836, \quad \frac{\beta_{\perp p}}{\beta_{\parallel p}} = 1, \quad \beta_{\parallel p} = 1, \\ &u_h = 1.9, \quad u_c = \frac{\delta u_h}{1-\delta}, \quad \frac{\beta_{\perp c}}{\beta_{\parallel c}} = 1, \quad \beta_{\parallel h} = 9, \\ &\frac{\beta_{\perp h}}{\beta_{\parallel h}} = 2 \text{ (Case 1)}, \quad 3.5 \quad \text{(Case 2)}, \quad 5 \quad \text{(Case 3)}. \end{aligned} \tag{17}$$

In the present study we focus only on the variation of temperature anisotropy associated with the halo electrons. Obviously, more systematic parametric survey can be done, but such a task is for future investigation.

Figure 1 displays the dispersion analysis in which normalized frequency, $z_r = \omega_k/\Omega_p$, and growth rate, $z_i = \gamma_k/\Omega_p$, are plotted against the normalized wave number, $q = ck/\omega_{pp}$, for the three cases listed above. We have solved for both forward propagating R mode (red) and backward propagating R (or equivalently, negative frequency L) mode (blue) over positive range of wave number k. However, once the solutions are obtained, we have invoked the symmetry relationship (11) and plotted the negative frequency L mode over negative k space. The left-hand panel of Figure 1 plots the real frequency of both branches of whistler, that is, backward (blue) and forward (red) modes, over the entire range of k values. Following the same pattern,

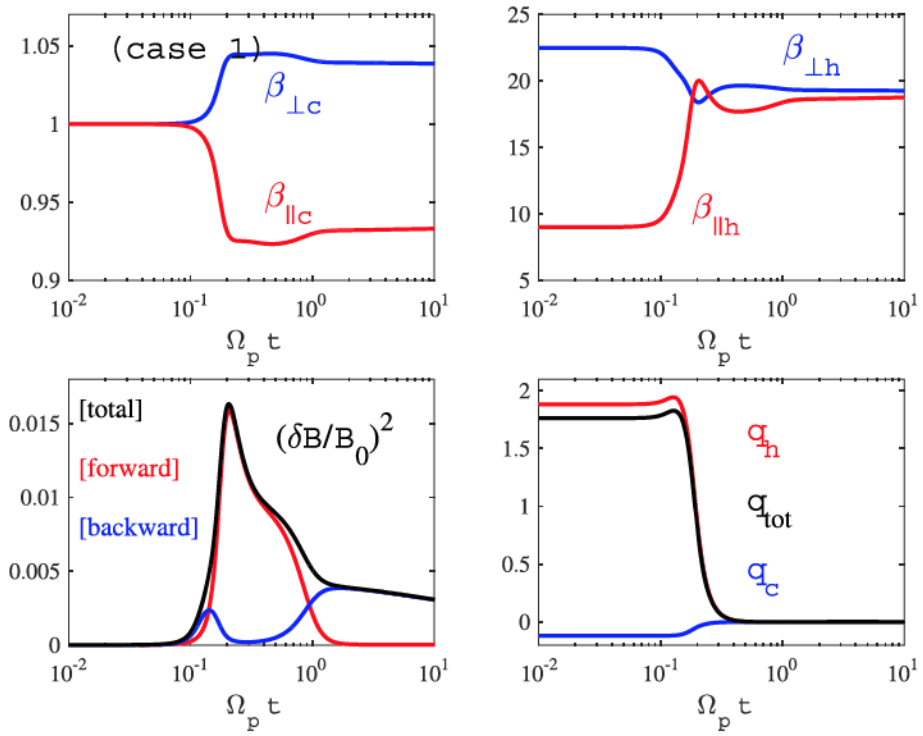

Figure 2. Evolution of bulk parameters and wave energy density for case 1. (top left) betas for core electrons, (top right) betas for halo electrons, (bottom left) wave magnetic field energy density, and (bottom right) heat flux.

the right-hand panel plots the corresponding growth rates. The forward versus backward modes are defined in the sense of these modes being characterized with either positive or negative k ranges. For case 3, the backward propagating mode dips below negative frequency over a limited range of wave numbers, which complicates the exact interpretation of the polarization and helicity. In our designation, however, forward versus backward waves simply means whether these modes occupy $k > 0$ or $k < 0$ domains. three different cases are indicated by solid (Case 1), dots (Case 2), and dash-dotted curves (Case 3). As a result of finite relative drift combined with temperature anisotropy associated with halo electrons, that is, $T_{\perp h}/T_{\parallel h}$ ranging from 2.5 (Case 1) to 3.5 (Case 2) and to 5 (Case 3), the forward versus backward combined WHF and EMEC modes have different dispersive properties, which includes asymmetric wave growth rates. Note that Case 3 with the highest halo temperature anisotropy has higher backward growth rate while Case 1 has somewhat comparable growth rate maxima for both modes. From this, one might be tempted to make the conjecture that for Case 3, the backward WHF mode might dominate in the saturation stage, while for case 1, the two modes will have comparable saturation wave intensities, case 2 being the intermediate situation. However, as we shall see next, quasi-linear evolution is quite distinct from such naive expectations based upon linear theory.

Figure 2 thus shows the time evolution of plasma bulk parameters as well as the wave intensities calculated with the quasi-linear method corresponding to Case 1. In the top two panels, we plot the time evolution of perpendicular and parallel core electron betas, $\beta_{\perp c}$ and $\beta_{\parallel c}$ (top left), as well as perpendicular and parallel halo electron betas, $\beta_{\perp h}$ and $\beta_{\parallel h}$ (top right), versus normalized time $\Omega_p t$. It is seen that the initially isotropic core electrons are heated in perpendicular direction while undergoing parallel cooling. As for the halo component, $\beta_{\perp h}$ initially decreases but subsequently it undergoes slight increase again before it settles down to the saturate value. Similarly, $\beta_{\parallel h}$ undergoes first increase until it reaches the peak value, followed by gradual decrease.

The bottom left panel of Figure 2 plots the forward (red) and backward (red) magnetic field wave energy densities, $\delta B^2/B_0^2$. We reiterate that the designation of forward and backward is in the sense as defined in Figure 1, that is, whether they occupy positive or negative k space. According to linear theory for the present Case 1, the forward and backward waves have comparable growth rates. Indeed, in the exponential growth

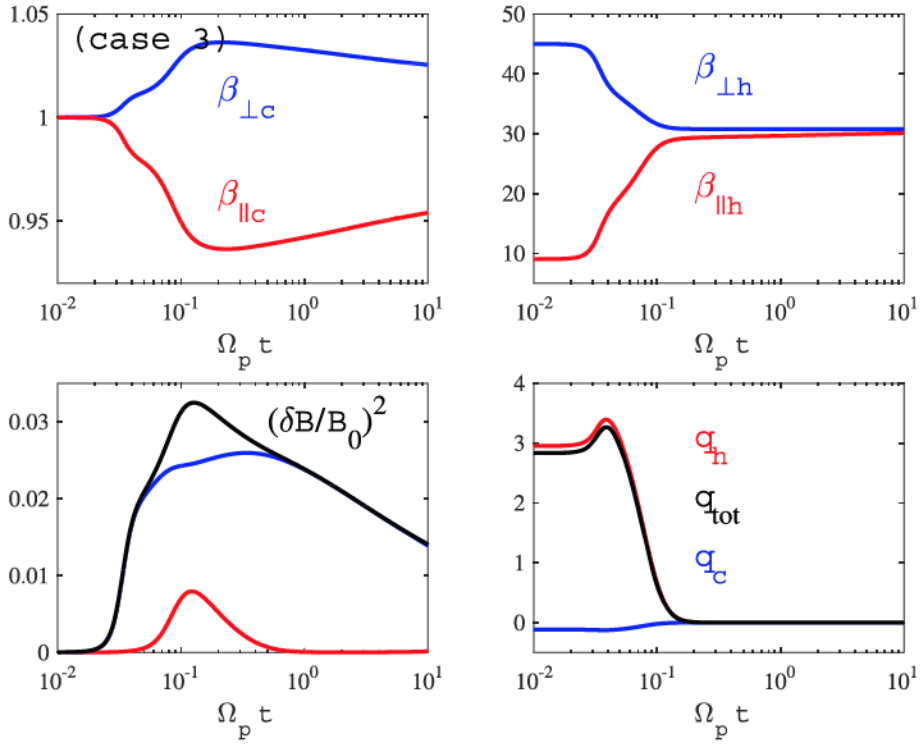

Figure 3. Evolution of bulk parameters and wave energy density for Case 3 in the same format as in Figure 2, which represents the situation where initially the backward mode grows much faster than the forward mode.

phase, it can be seen that the red and blue curves have indeed comparable rates of increase. However, rather unexpectedly, the backward mode subsequently undergoes damping, while the forward whistler mode dominates the intermediate state. However, over longer time scale, the forward mode is absorbed back by the plasma, while the backward mode increases again such that in the saturation stage, it is the backward mode that completely dominates the wave intensity. Nevertheless, the forward wave had already made the dominant contribution to the change in bulk plasma parameters during the intermediate stage such that the contributions from each mode has a complicated pattern at each stage of quasi-linear evolution. The black curve plots the sum of two intensities, and it indicates the relative contributions of each mode during different stages of evolution. This interplay of forward versus backward modes is quite complex, which defies any simple explanation based upon linear theory.

Note the peculiar feature associated with the backward waves. That is, the backward whistler mode waves first undergo excitation and damping, but in the late stage of evolution, the amplitude for these waves undergo increase again. The exact cause for the secondary increase of the backward waves in the nonlinear stage is not entirely clear, but judging from the particle behavior, it might be related to the perpendicular heating (and accompanying parallel cooling) associated with the core electrons, which promote the excitation of EMEC instability. Of course, such an explanation is not completely satisfactory since the anisotropy associated with the core electrons should also promote the increase of forward whistler waves as well. That is, the core temperature anisotropy should lead to reexcitation of both forward and backward waves. Nevertheless, the forward waves at this stage has undergone reabsorption by the particles. The cause cannot be related to any processes involving nonlinear decay, since we do not have such physics within the present quasi-linear scheme.

Finally, the bottom-right panel of Figure 2 shows the heat flux time evolution, where we plotted individual contributions from core and halo electrons as well as the net heat flux. The present quasi-linear analysis of the combined WHF and EMEC instability thus confirms that the collective instability plays an important role in regulating the heat flux in the solar wind.

According to the linear theory, Case 3 corresponds to the situation where the backward mode has much higher growth rate, while Case 2 is an intermediate case. Let us examine Case 3 first. Figure 3 plots the result,

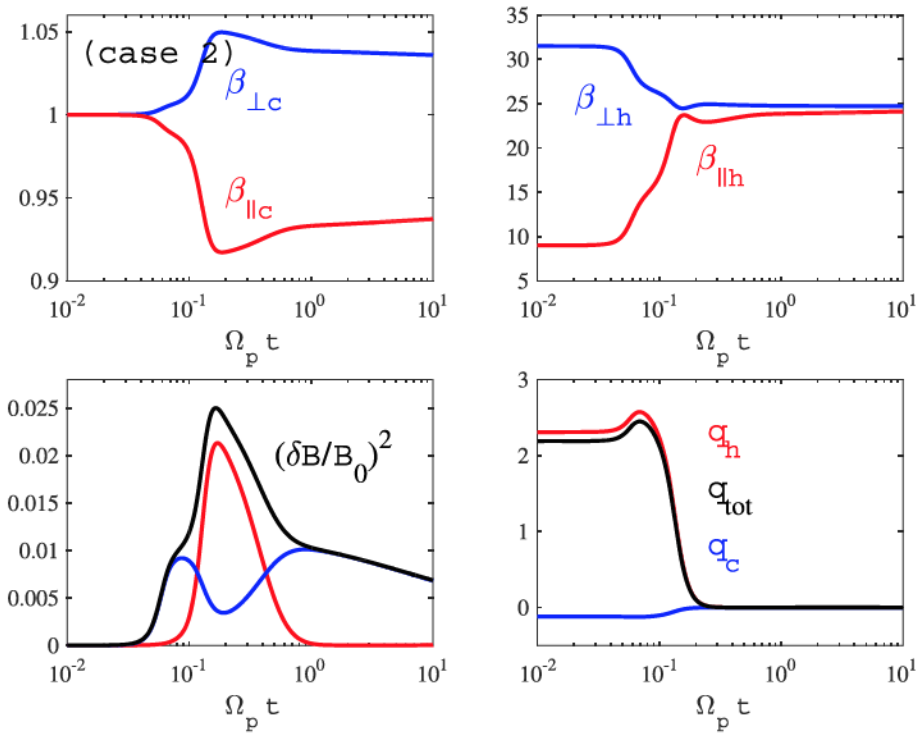

Figure 4. Evolution of bulk parameters and wave energy density for Case 2, which represents an intermediate situation, in the same format as in Figure 2.

which is in the same format as in Figure 2. In this case, the evolution of bulk parameters is quite similar to Case 1 in that initially isotropic core electrons undergo perpendicular heating and parallel cooling, while initially anisotropic halo electrons are isotropized by reduction of perpendicular beta and simultaneous increase of parallel beta. The heat flux evolution is also qualitatively similar. The noteworthy fact is that the wave energy evolution follows the dictates of linear theory in that the backward mode grows at a faster rate and maintains higher intensity throughout the entire time period. The forward mode, which grows at a slower rate, does increase to a finite but lower level at later time, but subsequently, is absorbed back by the particles. In this regard, for Case 3 at least, linear theoretical prediction is accurate in a qualitative sense. That is, the backward mode with higher growth rate dominates the quasi-linear evolution.

We now examine the quasi-linear evolution of physical quantities for Case 2, which is intermediate to Cases 1 and 3. Figure 4 plots the numerical result, which is in the same format as in Figure 2. Again, for this case too, the evolution of bulk parameters is quite similar to Cases 1 and 3 in that initially isotropic core electrons undergo perpendicular heating and parallel cooling, and initially anisotropic halo electrons undergo the opposite process of perpendicular cooling and parallel heating. Again, the time evolution of heat flux is also quite similar to the other two cases. As far as the time evolution of wave energy goes, this situation is indeed intermediate in that during the entire time evolution period, both forward and backward whistler modes contribute significantly, but at different stages in time. During the early period, the backward whistler mode wave, with its higher initial growth rate, increases in magnitude first and dominate the early dynamics. However, the forward mode, despite growing at a slower pace, dominates the middle stage of time evolution. It is noteworthy that, as in the previous two cases, the forward mode subsequently undergoes reabsorption by the particles and saturates at an extremely low intensity in the asymptotic stage. In the late time period, the backward mode, which had suffered an appreciable reduction in amplitude during the middle stage in time, grows again in amplitude. This behavior is similar to that of Case 1, except that in Case 1, the backward mode amplitude had been reduced to very low intensity before intensifying again. For the present Case 2, while the backward mode did undergo reduction during the middle stage, its amplitude had remained finite. In the late stage of evolution, it is seen that the backward mode completely dominates the saturation stage. Again, this is similar to Case 1. For Case 3, on the other hand, the backward mode never really underwent any appreciable reduction in amplitude throughout the entire quasi-linear evolution. Such a complex interplay

between the forward and backward waves for the three case investigated could not have been foreseen simply based on linear calculation. This shows that the solar wind heat flux or anisotropy instability requires at a minimum, quasi-linear analysis.

4. Summary and Discussion

Isotropic states of solar wind plasma species had been reported in a series of space observations that show significant deviations from the predictions of classical Chew-Goldberger-Low relations (Chew et al., 1956). Heat flux, collision between solar wind species, and instabilities driven by the temperature anisotropy are the three key factors which define the state of solar wind temperatures. For a magnetized and noncollisional interplanetary plasma, different species (protons, electrons, and alpha particles) can easily develop the heat flux and temperature anisotropies as a result of expansion, which may drive the system to an unstable state. Under the aforementioned condition, the microinstabilities appear to contribute appreciably, and lead the solar wind toward marginal instability threshold condition. The present study explores the dynamical evolutions of combined WHF and EMEC instabilities, which are driven by different free sources. WHF instability is driven by the relative drift between the core and halo electrons (in the proton rest frame), and the excitation of WHF instability leads to the inhibition of the heat flux in the solar wind as well as to alter the degree of temperature anisotropies. The temperature anisotropy-driven EMEC instability primarily affect the reduction of temperature anisotropy or perpendicular heating.

The main focus of the present paper had been in the role of forward versus backward propagating unstable whistler mode waves in the dynamics of solar wind plasma. The forward propagating WHF instability is asymmetrically excited, while the temperature anisotropy-driven EMEC instability is symmetrically excited in the absence of relative drift. The combined WHF and EMEC generally leads to bidirectional excitation of whistler mode waves, but simple linear theory cannot always predict the nonlinear development of the instability. We have considered three sample cases where in the first case, initial growth rates associated with forward versus backward waves are somewhat comparable. However, quasi-linear calculation shows that only during the very early stage of instability development do the two modes grow at comparable rates. Subsequent to the exponential growth phase, the backward mode suddenly underwent reduction while the forward mode almost completely dominated the dynamics. This is shown in Figure 2. From this, it was quite evident that the forward mode is the more important mode of the two, and it provides some justification of ignoring the backward mode excitation in the quasi-linear calculation as carried out by Shaaban et al. (2019a) and Shaaban et al. (2019b).

When we consider the situation where the backward mode has a much higher growth rate, as in Case 3, both linear theory and quasi-linear calculation shows that the backward propagating whistler mode dominates the entire dynamics. This is shown in Figure 3. For this case, had one considered only the forward propagating whistler mode, then one would have obtained a completely incorrect result. For an intermediate situation (Case 2), which is depicted in Figure 4, both forward and backward mode had different but equally important dynamical contributions during distinct stages of time evolution. Again, for parameter regime as in Case 2, it would be quite incorrect to ignore the excitation of backward propagating whistler mode wave.

The present findings, while interesting, must be confirmed with more rigorous simulations, which is beyond the scope of the present work. However, we hasten to point out that a recent implicit PIC code simulation by López, Shaaban, et al. (2019) demonstrated that the quasi-linear moment calculation is in qualitative agreement with the simulation. In a recent work Lee et al. (2019) carried out the explicit PIC simulation of heat flux instability in one dimension assuming parallel/antiparallel propagation of the heat flux instability. However, the initial condition for their simulation is relevant for fire hose (that is, left-hand circularly polarized) heat flux instability, rather than the whistler heat flux instability, which is a right-hand mode. The linear theory of firehose heat flux instability was recently discussed by Saeed, Sarfraz, et al. (2017), Saeed, Yoon, et al. (2017) and Shaaban, Lazar, Yoon, et al. (2018).

Besides the assumption of self-similar drifting bi-Maxwellian model, we have also made the assumption that the most important wave modes are those that propagate in parallel (forward) or antiparallel (backward) directions. Of course, such an assumption must be verified, say by a more general two- or three-dimensional quasi-linear analysis, or higher-dimensional simulations. A recent work by López et al. (2019) is of relevance in this regard. While their two-dimensional PIC code simulation pertains to the oblique electron fire

hose instability driven by a single component electrons with excessive parallel temperature anisotropy, the oblique heat flux instability may also be simulated by means of the same method.

Further, we have restricted ourselves for slow solar wind conditions at heliocentric distances near Earth orbit. Under these limits, we modeled both core and halo electron components with bi-Maxwellian form of distributions. One could invoke a more general study at different radial distances at which the observed halo electron component is best modeled by Kappa distribution (Maksimovic et al., 2005), (Štverák et al., 2008) as employed in many earlier theoretical works such as those by Lazar et al. (2014), Lazar et al. (2015), and Shaaban et al. (2016). The threshold conditions may significantly be changed with the inclusion of obliqueness in the propagation as for the case of electron fire hose instability (Li & Habbal, 2000; Gary & Nishimura, 2003).

To summarize, despite some caveats and limitations as already mentioned above, we report for the first time, the study of linear and quasi-linear analyses for backward and forward propagating WHF and EMEC instabilities. In principle, the extension of this work to two (or three) dimensions of propagation can be done in the future. Introducing the effects of inhomogeneities in the system, that is, the radial expansion effects, to the present approach of macroscopic quasi-linear analysis can also be attempted in the future. Such a task will lead to a significant improvement in the existing global-kinetic solar wind models (Chandran et al., 2011; Denton et al., 1994; Hellinger & Trávníček, 2008; Yoon & Seough, 2014; Yoon & Sarfraz, 2017).

Acknowledgments
The present paper does not involve any spacecraft data analysis. P. H. Y. acknowledges NASA Grant NNH18ZDA001N-HSR and NSF Grant 1842643 to the University of Maryland.

References

Bertschinger, E., & Meiksin, A. (1986). The role of heat conduction in the cooling flows of galaxy clusters *Asrtophys. Astrophysical Journal Letters*, *306*, L1–L5. https://doi.org/10.1086/184692

Chandran, B. D. G., Dennis, T. J., Quataert, E., & Bale, S. D. (2011). Incorporating kinetic physics into a two-fluid solar-wind model with temperature anisotropy and low-frequency Alfvén-wave turbulence. *The Astrophysical Journal*, *734*, 197. https://doi.org/10.1088/0004-637X/743/2/197

Chew, G. F., Goldberger, M. L., & Low, F. E. (1956). The Boltzmann equation and the one-fluid hydromagnetic equations in the absence of particle collisions. *Proceedings of the Royal Society of London. Series A*, *236*, 112. https://doi.org/10.1098/rspa.1956.0116

Cowie, L. L., & McKee, C. F. (1977). The evaporation of spherical clouds in a hot gas. I - Classical and saturated mass loss rates. *The Astrophysical Journal*, *211*, 135–146. https://doi.org/10.1086/154911

Denton, R. E., Anderson, B. J., Gary, S. P., & Fuselier, S. A. (1994). Bounded anisotropy fluid model for ion temperature. *Journal of Geophysical Research*, *99*, 11,225. https://doi.org/10.1029/94JA00272

Fabian, A. C. (1994). Cooling flows in clusters of galaxies. *Astronomy and Astrophysics*, *32*, 277. https://doi.org/10.1146/annurev.aa.32.090194.001425

Fang, X.-E., Guo, F., Yuan, Y.-F., & Mou, G. (2018). On the efficiency of thermal conduction in galaxy clusters. *The Astrophysical Journal*, *863*, 177.

Fried, B., & Conte, S. D. (1961). *The Plasma Dispersion Function*. New York: Academic Press.

Gary, S. P. (1985). Electromagnetic electron beam instabilities: Hot, isotropic beams. *Journal of Geophysical Research*, *90*, 10,815–10,822. https://doi.org/10.1029/JA090iA11p10815

Gary, S. P. (1993). *Theory of Space Plasma Microinstabilities*. New York: Cambridge University Press.

Gary, S. P., & Feldman, W. C. (1977). Solar wind heat flux regulation by the Whistler instability. *Journal of Geophysical Research*, *82*, 1087. https://doi.org/10.1029/JA082i007p01087

Gary, S. P., Feldman, W. C., Forslund, D. W., & Montgomery, M. D. (1975). Heat flux instabilities in the solar wind. *Journal of Geophysical Research*, *80*, 4197. https://doi.org/10.1029/JA080i031p04197

Gary, S. P., & Li, H. (2000). Whistler heat flux instability at high beta. *The Astrophysical Journal*, *529*, 1131. https://doi.org/10.1086/308294

Gary, S. P., & Nishimura, K. (2003). Resonant electron firehose instability: Particle-in-cell simulations. *Physics of Plasmas*, *10*, 3571. https://doi.org/10.1063/1.1590982

Gary, S. P., Scime, E. E., Phillips, J. L., & Feldman, W. C. (1994). The whistler heat flux instability: Threshold conditions in the solar wind. *Journal of Geophysical Research*, *99*, 23,391–23,399. https://doi.org/10.1029/94JA02067

Gary, S. P., Skoug, R. M., & Daughton, W. (1999). Electron heat flux constraints in the solar wind. *Physics of Plasmas*, *6*, 2607. https://doi.org/10.1063/1.873532

Gary, S. P., Vazquez, V. M., & Winske, D. (1996). Electromagnetic proton cyclotron instability: Proton velocity distributions. *Journal of Geophysical Research*, *101*, 13,327–13,333. https://doi.org/10.1029/96JA00295

Hellinger, P., & Trávníček, P. M. (2008). Oblique proton fire hose instability in the expanding solar wind: Hybrid simulations. *Journal of Geophysical Research*, *113*, A10109. https://doi.org/10.1029/2008JA013416

Hellinger, P., Trávníček, P. M., Decyk, V. K., & Schriver, D. (2014). Oblique electron fire hose instability: Particle-in-cell simulations. *Journal of Geophysical Research: Space Physics*, *119*, 59–68. https://doi.org/10.1002/2013JA019227

Komarov, S., Schekochihin, A. A., Churazov, E., & Spitkovsky, A. (2018). Self-inhibiting thermal conduction in a high-β, whistler-unstable plasma. *Journal of Plasma Physics*, *84*. https://doi.org/10.1017/S0022377818000399

Lazar, M., Poedts, S., & Schlickeiser, R. (2014). The interplay of Kappa and core populations in the solar wind: Electromagnetic electron cyclotron instability. *Journal of Geophysical Research: Space Physics*, *119*, 9395–9406. https://doi.org/10.1002/2014JA020668

Lazar, M., Poedts, S., Schlickeiser, R., & Dumitrache, C. (2015). Towards realistic parametrization of the kinetic anisotropy and the resulting instabilities in space plasmas. Electromagnetic electron-cyclotron instability in the solar wind. *Monthly Notices of the Royal Astronomical Society*, *446*, 3022–3033. https://doi.org/10.1093/mnras/stu2312

Lee, S.-Y., Lee, E., & Yoon, P. H. (2019). Nonlinear development of electron heat flux instability: Particle in cell simulation. *The Astrophysical Journal*, *876*, 117. https://doi.org/10.3847/1538-4357/ab12db

Li, X., & Habbal, S. R. (2000). Electron kinetic firehose instability. *Journal of Geophysical Research*, *105*, 27,377–27,385. https://doi.org/10.1029/2000JA000063

López, R. A., Lazar, M., Shaaban, S. M., Poedts, S., Yoon, P. H., Viñas, A. F., & Moya, P. S. (2019). Particle-in-cell simulations of firehose instability driven by bi-Kappa electrons. *The Astrophysical Journal Letters*, *873*, L20. https://doi.org/10.3847/2041-8213/ab0c95

López, R. A., Shaaban, S. M., Lazar, M., Poedts, S., Yoon, P. H., Micera, A., & Lapenta, G. (2019). Particle-in-cell simulations of the whistler heat-flux instability in the solar wind conditions. *The Astrophysical Journal Letters*, *882*, L8. https://doi.org/10.3847/2041-8213/ab398b

Maksimovic, M., Zouganleis, I., Chaufray, J.-Y., Issautier, K., Scime, E. E., Littleton, J. E., et al. (2005). Radial evolution of the electron distribution functions in the fast solar wind between 0.3 and 1.5 AU. *Journal of Geophysical Research*, *110*, A09104. https://doi.org/10.1029/2005JA011119

Maneva, Y., Lazar, M., Viñas, A., & Poedts, S. (2016). Mixing the solar wind proton and electron scales: Effects of electron temperature anisotropy on the oblique proton firehose instability. *The Astrophysical Journal*, *832*, 64. https://doi.org/10.3847/0004-637X/832/1/64

Matteini, L., Landi, S., Hellinger, P., & Velli, M. (2006). Parallel proton fire hose instability in the expanding solar wind: Hybrid simulations. *Journal of Geophysical Research*, *111*, A10101. https://doi.org/10.1029/2006JA011667

Michno, M. J., Lazar, M., Yoon, P. H., & Schlickeiser, R. (2014). Effects of electrons on the solar wind proton temperature anisotropy. *The Astrophysical Journal*, *781*, 49. https://doi.org/10.1088/0004-637X/781/1/49/meta

Parker, E. N. (1964). Dynamical properties of stellar coronas and stellar winds. II. Integration of the heat-flow qquation. *The Astrophysical Journal*, *139*(93). https://doi.org/10.1086/147741

Pilipp, W. G., Miggenrieder, H., Montgomery, M. D., Mühlhäuser, K.-H., Rosenbauer, H., & Schwenn, R. (1987). Unusual electron distribution functions in the solar wind derived from the Helios plasma experiment: Double-strahl distributions and distributions with an extremely anisotropic core. *Journal of Geophysical Research*, *92*, 1093–1101. https://doi.org/10.1029/JA092iA02p01093

Pistinner, S. L., & Eichler, D. (1998). Self-inhibiting heat flux. *Monthly Notices of the Royal Astronomical Society*, *301*, 49. https://doi.org/10.1046/j.1365-8711.1998.01770.x

Pontieu, B. D., McIntosh, S. W., Carlsson, M., Hansteen, V. H., Tarbell, T. D., Boerner, P., et al. (2011). The Origins of hot plasma in the solar corona. *Science*, *331*, 55. https://doi.org/10.1126/science.1197738

Saeed, S., Sarfraz, M., Yoon, P. H., Lazar, M., & Qureshi, M. N. S. (2017). Electron heat flux instability. *Monthly Notices of the Royal Astronomical Society*, *465*, 1672. https://doi.org/10.1093/mnras/stw2900

Saeed, S., Yoon, P. H., Sarfraz, M., & Qureshi, M. N. S. (2017). Characteristics of heat flux and electromagnetic electron-cyclotron instabilities driven by solar wind electrons. *Monthly Notices of the Royal Astronomical Society*, *121*, 9356. https://doi.org/10.1093/mnras/stx049

Sarfraz, M. (2018). A moment-based quasilinear theory for electron firehose instability driven by solar wind core/halo electrons. *Journal of Geophysical Research: Space Physics*, *123*, 6107–6618. https://doi.org/10.1029/2018JA025449

Sarfraz, M., Saeed, S., Yoon, P. H., Abbas, G., & Shah, H. A. (2016). Macroscopic quasi-linear theory of electromagnetic electron cyclotron instability associated with core and halo solar wind electrons. *Journal of Geophysical Research: Space Physics*, *121*, 9356–9368. https://doi.org/10.1002/2016JA022854

Sarfraz, M., & Yoon, P. H. (2019). Contributions of protons in electron firehose instability driven by solar wind core-halo electrons. *Monthly Notices of the Royal Astronomical Society*, *486*, 3550–3559. https://doi.org/10.1093/mnras/stz1086

Schilckeiser, R. (2002). *Cosmic Ray Astrophysics*. Berlin: Springer.

Seough, J., & Yoon, P. H. (2012). Quasilinear theory of anisotropy-beta relations for proton cyclotron and parallel firehose instabilities. *Journal of Geophysical Research*, *117*, A08101. https://doi.org/10.1029/2012JA017645

Seough, J., Yoon, P. H., & Hwang, J. (2014). Quasilinear theory and particle-in-cell simulation of proton cyclotron instability. *Physics of Plasmas*, *21*, 062118. https://doi.org/10.1063/1.4885359

Seough, J., Yoon, P. H., & Hwang, J. (2015). Simulation and quasilinear theory of proton firehose instability. *Physics of Plasmas*, *22*, 012303. https://doi.org/10.1063/1.4905230

Seough, J., Yoon, P. H., Kim, K.-H., & Lee, D. H. (2013). Solar-wind proton anisotropy versus beta relation. *Physical Review Letters*, *110*, 071103. https://doi.org/10.1103/PhyRevLett.110.071103

Shaaban, S. M., Lazar, M., & Poedts, S. (2018). Clarifying the solar wind heat flux instabilities. *Monthly Notices of the Royal Astronomical Society*, *480*, 310–319. https://doi.org/10.1093/mnras/sty1567

Shaaban, S. M., Lazar, M., Poedts, S., & Elhanbaly, A. (2016). The interplay of the solar wind proton core and halo populations: EMIC instability. *Journal of Geophysical Research: Space Physics*, *121*, 6031–6047. https://doi.org/10.1002/2016JA022587

Shaaban, S. M., Lazar, M., Poedts, S., & Elhanbaly, A. (2017). Shaping the solar wind temperature anisotropy by the interplay of electron and proton instabilities. *Astrophysics and Space Science*, *362*, 13. https://doi.org/10.1007/s10509-016-2994-7

Shaaban, S. M., Lazar, M., Yoon, P. H., & Poedts, S. (2018). Beaming electromagnetic (or heat-flux) instabilities from the interplay with the electron temperature anisotropies. *Physics of Plasmas*, *25*, 082105. https://doi.org/10.1063/1.5042481

Shaaban, S. M., Lazar, M., Yoon, P. H., & Poedts, S. (2019a). Quasi-linear approach of the whistler heat-flux instability in the solar wind. *Monthly Notices of the Royal Astronomical Society*, *486*, 4498–4507. https://doi.org/10.1093/mnras/stz830

Shaaban, S. M., Lazar, M., Yoon, P. H., & Poedts, S. (2019b). Quasilinear approach of the cumulative whistler instability in fast solar wind: Constraints of electron temperature anisotropy. *Astronomy and Astrophysics*, *627*, A76. https://doi.org/10.1051/0004-6361/201935515

Štverák, Š., Maksimovic, M., Trávníček, P. M., Marsch, E., Fazakerley, A. N., & Scime, E. E. (2009). Radial evolution of nonthermal electron populations in the low-latitude solar wind: Helios, Cluster, and Ulysses Observations. *Journal of Geophysical Research*, *114*, A05104. https://doi.org/10.1029/2008JA013883

Štverák, Š., Trávníček, P., Maksimovic, M., Marsch, E., Fazakerley, A. N., & Scime, E. E. (2008). Electron temperature anisotropy constraints in the solar wind. *Journal of Geophysical Research*, *113*, A03103. https://doi.org/10.1029/2007JA012733

Tong, Y., Bale, S. D., Salem, C., & Pulupa, M. (2018). Observed instability constraints on electron heat flux in the solar wind. arXiv e-prints. https://arxiv.org/abs/1801.07694

Tong, Y., Vasko, I. Y., Pulupa, M., Mozer, F. S., Bale, S. D., Artemyev, A. V., & Krasnoselskikh, V. (2019). Whistler wave generation by halo electrons in the solar wind. *The Astrophysical Journal Letters*, *870*, L6. https://doi.org/10.3847/2041-8213/aaf734

Vasko, I. Y., Krasnoselskikh, V., Tong, Y., Bale, S. D., Bonnell, J. W., & Mozer, F. S. (2019). Whistler fan instability driven by strahl electrons in the solar wind. *The Astrophysical Journal Letters*, *871*, L29. https://doi.org/10.3847/2041-8213/ab01bd

Wagh, B., Sharma, P., & McCourt, M. (2014). Thermal conduction and multiphase gas in cluster cores. *Monthly Notices of the Royal Astronomical Society*, *439*, 2822–2827. https://doi.org/10.1093/mnras/stu138

Yoon, P. H., López, R. A., Seough, J., & Sarfraz, M. (2017). Velocity moment-based quasilinear theory and particle-in-cell simulation of parallel electron firehose instability. *Physics of Plasmas*, *24*, 112104. https://doi.org/10.1063/1.4997666

Yoon, P. H., & Sarfraz, M. (2017). Interplay of electron and proton instabilities in expanding solar wind. *The Astrophysical Journal*, *835*, 246. https://doi.org/10.3847/1538-4357/835/2/246

Yoon, P. H., & Seough, J. (2012). Quasilinear theory of anisotropy-beta relation for combined mirror and proton cyclotron instabilities. *Journal of Geophysical Research*, *117*, A08102. https://doi.org/10.1029/2012JA017697

Yoon, P. H., & Seough, J. (2014). Proton-cyclotron and firehose instabilities in inhomogeneous plasmas. *Journal of Geophysical Research*, *119*, 7108. https://doi.org/10.1029/2014JA020261

Yoon, P. H., Seough, J., Hwang, J., & Nariyuki, Y. (2015). Macroscopic quasi-linear theory and particle-in-cell simulation of helium ion anisotropy instabilities. *Journal of Geophysical Research: Space Physics*, *120*, 6071–6084. https://doi.org/10.1002/2015JA021495

Zakamska, N. L., & Narayan, R. (2003). Models of galaxy clusters with thermal conduction. *The Astrophysical Journal*, *582*, 162. https://doi.org/10.1086/344641